ELECTRONIC SUPPLEMENTARY INFORMATION:

Physical aging of polymers of intrinsic microporosity: a SAXS/WAXS study

Amanda G. McDermott,[a†] Peter M. Budd,[b] Neil B. McKeown,[c‡] Coray M. Colina[a]
and James Runt[a]

[a] Department of Materials Science and Engineering, The Pennsylvania State University, University Park, PA 16802. Corresponding email: runt@matse.psu.edu.
[b] School of Chemistry, The University of Manchester, Manchester, M13 9PL, UK.
[c] School of Chemistry, Cardiff University, CF10 3AT, UK.
[†] Present address (AGM): Materials Science and Engineering Division, National Institute of Standards and Technology, Gaithersburg, MD 20899; amanda.mcdermott@nist.gov.
[‡] Present address (NBM): School of Chemistry, University of Edinburgh, Edinburgh, Scotland EH9 3JJ.

CONTENTS

ESI-1. Additional experimental data supporting interpretation of PIM scattering features: WAXS data from powder PIMs of varied chemistries, and USAXS data from PIM-1 with varied sample histories and other amorphous homopolymers.

ESI-2. Two attempts at modeling PIM scattering data—hard-sphere and bicontinuous Teubner-Strey—which support the association of the broad SAXS feature with porosity but are not quantitatively satisfactory.

ESI-3. Detailed PIM scattering data from the aging study, showing excellent overlap between SAXS and WAXS patterns. The partial scattering invariant with alternate integration ranges is also shown.

ESI-4. Details of simulated PIM-1 boxes.

ESI-1. ADDITIONAL EXPERIMENTAL SCATTERING DATA

ESI-1.1 WAXS: Powder PIMs of Varied Chemistries

WAXS patterns from powder samples of several variants of PIM-1 were collected (chemical structures Figure ESI-1; WAXS patterns Figure ESI-2). In most cases only small quantities were available (~2 to 15 mg) and the polymers were insoluble (unlike PIM-1), so films could not be cast.

While wide-angle scattering from PIM films and powders is similar, in powders the broad SAXS feature is overwhelmed by very intense power-law scattering with onset near 0.2 $Å^{-1}$. This is typical of particulate materials and is indicative of the fractal nature of powder particle packing. Presumably the faster kinetics during precipitation compared to solvent-casting radically alter the polymer's organization beyond the local scale. As a consequence, the broad SAXS feature can only be meaningfully studied in films.

Small differences in the relative intensities of the weaker high-*q* features between films and powders have been noted[1]. In spite of these limitations, there are some interesting trends in high-*q* features resulting from alterations of PIM-1's spirocenter substituents as well as substitutions of nitrile groups.

Changing spirocenter methyl groups to the larger Ph or 2Ph (Figure ESI-2, top) gives rise to an additional peak (Table ESI-1) similar to the 15-Å segment length, which could be related to increased scattering contrast from larger groups separated by this characteristic distance. This structural change also influences the relative intensities—but not wavevectors—of other high-*q* features that do appear in PIM-1. This supports the idea, suggested by examination of partial simulated structure factors in previous work[1], that high-*q* features are related to the organization of the spirocenters, which function as sites of contortion along chains.

In contrast, changing nitrile groups to fluorines or pyridines, or creating crosslinks at nitrile sites, shifts the Bragg spacing of the ~7-Å feature by up to 1 Å (Figure ESI-2, bottom, and Table ESI-1), causing the distinct high-*q* features to merge together. These functional groups are more polar than any of the spirocenter substituent variants, so it is likely that they influence electrostatic interactions between chains. This would affect either intersegmental distances or characteristic distances between spirocenters, so this observation is less useful in discriminating between different interpretations of high-*q* features.

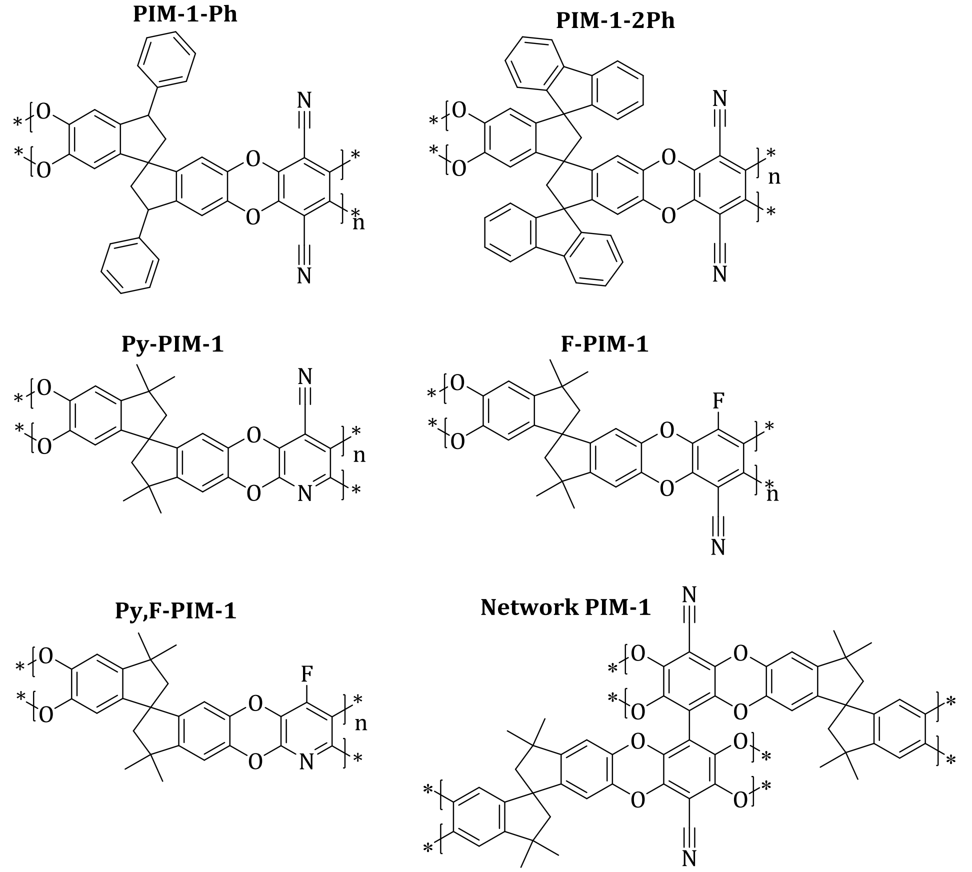

Figure ESI-1. Chemical structures of polymers of intrinsic microporosity (PIMs) with variant chemistries; synthesis reported previously[2]. Modifications to the nitrile group of PIM-1 are denoted with a prefix, while altered spirocenter substituents are named with a suffix.

Table ESI-1. Wavevectors and equivalent Bragg spacings of scattering features from powder samples of PIM-1 variants, indicated with dashed lines in Figure ESI-2.

Series	Polymer	*q* (Å-1)	*d* (Å)
Modified nitrile groups (Figure ESI-2, top)	PIM-1	0.91	6.9
	Network PIM-1	1.00	6.3
	Py-PIM-1	0.97	6.5
	F-PIM-1	0.91	6.9
	Py,F-PIM-1	1.05	6.0
Modified spirocenter substituents (Figure ESI-2, bottom)	PIM-1	-	-
	PIM-1-Ph	0.49	12.8
	PIM-1-2Ph	0.56	11.2

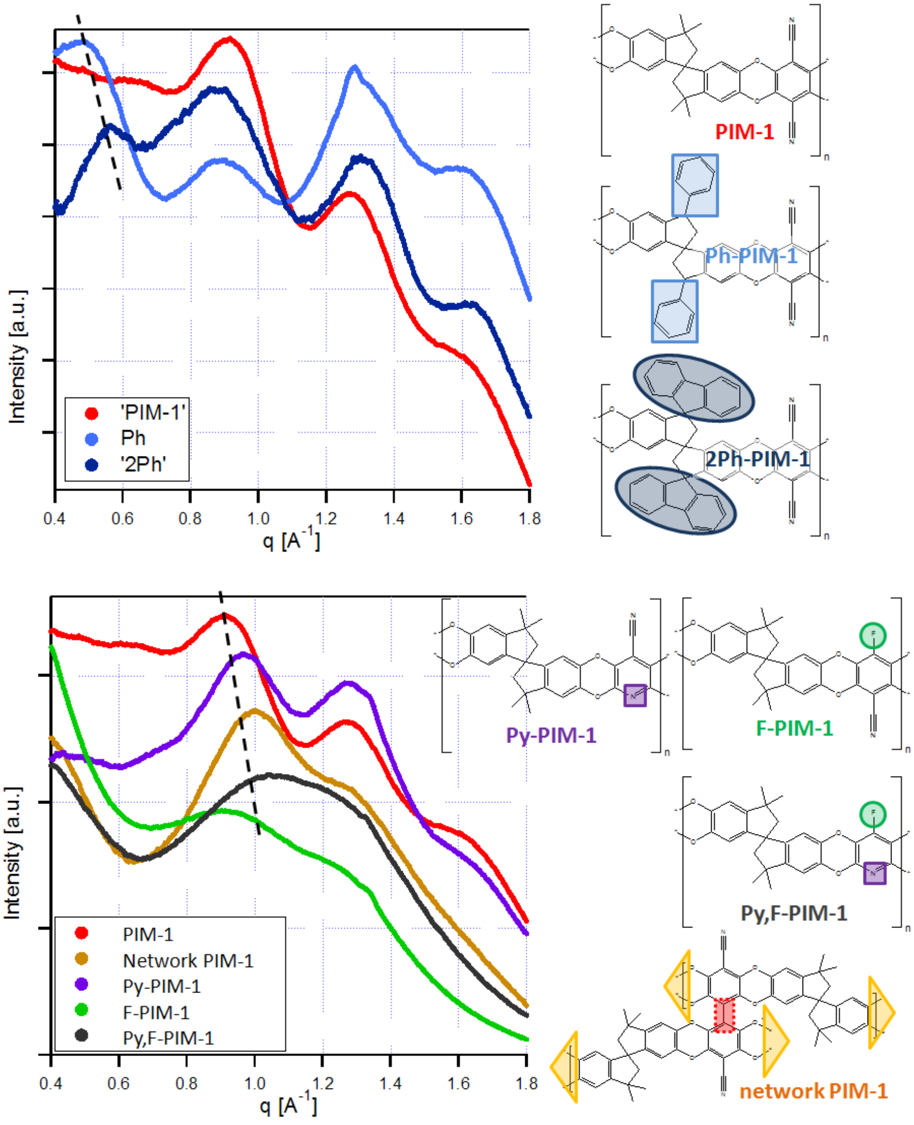

Figure ESI-2. WAXS patterns from (top) PIM-1 with modified spirocenter substituents and (bottom) PIM-1 with modified nitrile groups. Larger versions of the chemical structures on the right are shown in Figure ESI-1.

ESI-1.2 USAXS: PIM-1 with varied sample histories and compared to nonporous polymers

The origin of low-*q* power-law scattering in amorphous, neat homopolymers, of the form

$$I(q) \propto q^{-\alpha}$$

is in general poorly understood. Here it suffices to note that the upturn is present in a wide variety of *non*porous polymers and that in PIM-1, the intensity and exponent of this low-*q* scattering are within the range observed for nonporous amorphous polymers (Figure ESI-2a). In addition, this scattering feature is not sensitive to sample history, which certainly affects porosity (Figure ESI-2b).

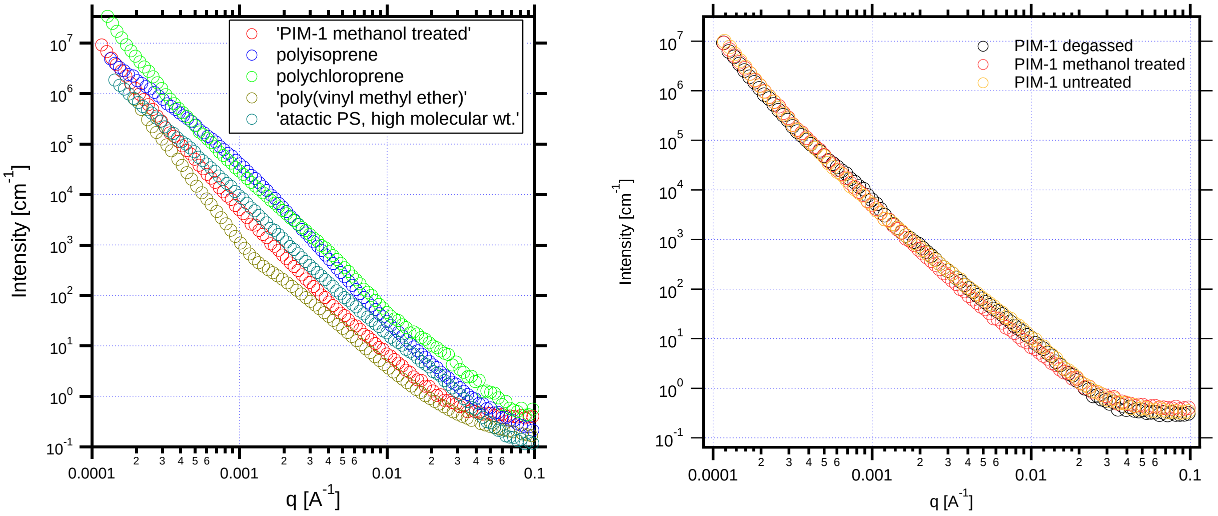

(a) **(b)**

Figure ESI-3. **(a)** USAXS patterns from PIM-1 (red) compared to assorted amorphous polymers. **(b)** USAXS patterns from PIM-1 films with different sample histories. The scattered intensity and q^{-3} power law are not sensitive to sample history.

Power-law scattering is frequently interpreted as a fractal dimension, with mass fractals giving rise to exponents α between 1 (sparse) and 3 (dense), and surface fractals giving rise to exponents between 3 (rough) and 4 (smooth)[3]. For smooth surfaces, the Porod equation relates specific surface area *S*/*V* to scattered intensity:

$$\lim_{q\to\infty} \frac{I(q)}{Q} = \frac{2\pi}{\varphi_1\varphi_2}\frac{S}{V}\frac{1}{q^4}$$

where φ_1 and φ_2 are the volume fractions of the two phases, and *Q* is the scattering invariant:

$$Q = \frac{1}{2\pi^2}\int_0^\infty q^2 I(q)dq$$

Although there are modified versions of the Porod equation suitable for diffuse surfaces, it is crucial to recognize that it represents the *high-q limit* of scattering from objects whose form factors (shapes and sizes) contribute to scattering at still lower *q*. Thus, a specific surface area calculated from PIM-1's low-*q* power-law scattering would describe the surface area of objects larger than several microns, not of pores smaller than 1-2 nm.

A specific surface area for PIMs could in principle be derived from data in the approximate range of 1 to 5 Å^{-1}, but there are two complications. First, it is unclear that the surface in question is 'smooth'—micropores are only a few times larger than the atoms that define the interior surface area and whose orbiting electrons determine their interaction radii. Second, a number of weak peaks are superimposed on this *hypothetical* high-*q* power-law scattering. In combination, these factors make fitting high-*q* PIM scattering data to the Porod law impractical.

ESI-2. MODELING PIM SCATTERING DATA

ESI-2.1 Failure of Simple Models for Porous and Two-Phase Materials

Typical scattering patterns from porous materials include power-law scattering at high q leveling off to flat scattering at low q [4]. The wavevector corresponding to the transition between these two scattering regimes depends on the size of the pores (Figure ESI-4, left). In the case of q^{-4} power-law scattering at high q, the Porod equation can be applied to extract a specific surface area, as discussed in ESI-1.2.

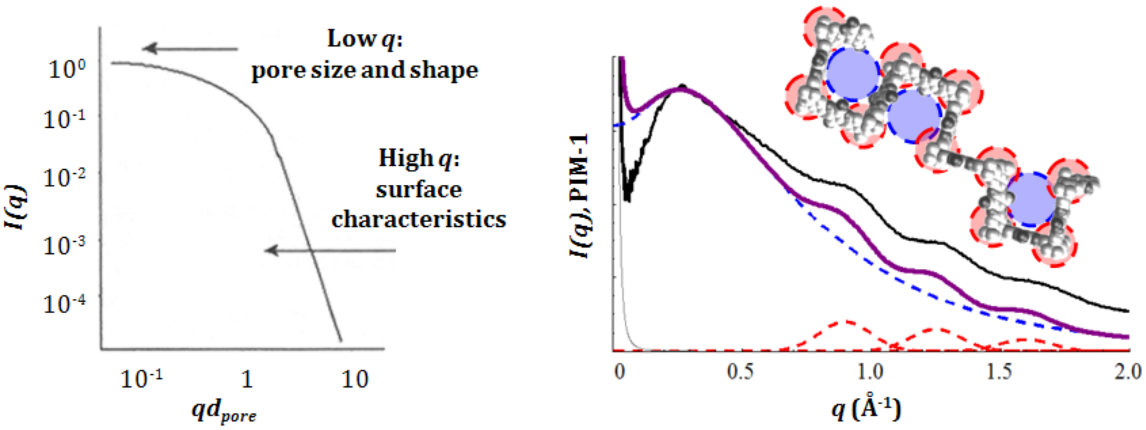

Figure ESI-4. Typical scattering patterns from porous materials (left) compared with scattering from PIM-1 (black line, right) along with model components suggested by the analysis in the main portion of the paper. The model (purple) is the sum of a q^{-3} term (grey, thin), three Gaussian peaks related to the local organization of spirocenters (red, dashed), and another term (blue, dashed) arising from the porosity. Possible functional forms of the porosity term are discussed in this section. The figure on the left is adapted from ref [4].

If pores are modeled as particles, a radius of gyration R_g can be determined by applying the Guinier equation[3] to low-q scattering data:

$$I(q) = \rho_0^2 v^2 e^{-\frac{1}{3}q^2 R_g^2} \qquad \text{(ESI-1)}$$

where v is the particle volume and ρ_0 is the scattering contrast.

If porosity is considered to be a continuous (nonparticulate) phase, a correlation length ξ can be determined using the Debye-Bueche equation[5, 6]:

$$I(q) = \frac{8\pi\langle\eta^2\rangle\xi^3}{(1 + q^2\xi^2)^2} \qquad \text{(ESI-2)}$$

where $\langle\eta^2\rangle$ is the average fluctuation in electron density between the two phases. This functional form can ideally be applied to the entire q range, encompassing flat scattering at low q and reducing to the Porod equation ($I \propto q^{-4}$) at high q.

Several difficulties arise when attempting to apply these models to scattering from PIM films. It can be argued that including the low-q q^{-3} scattering and the weak high-q peaks as additive terms (Figure ESI-4, right) is reasonable. However, neither Equation ESI-1 nor Equation ESI-2 can account for the broad SAXS maximum near q = 0.27 Å^{-1}, which has been established as closely related to porosity but not directly indicative of pore sizes.

Both particulate and nonparticulate models of greater complexity are examined below in an attempt to model the broad SAXS peak, treating PIM-1 as a two-phase system consisting of porosity (unoccupied volume) and polymer chains. Since neither is found to be quantitatively satisfactory, the scattering invariant is used in the main paper as a model-independent measure of porosity. However, the length scales required in each model to reproduce the broad SAXS maximum are similar to the sizes of pores measured by other techniques, lending further support to the association of this scattering feature with porosity.

ESI-2.2 Particulate Hard-Sphere Model

The equivalence of scattered intensity from a particulate system can be represented as the product of a form factor $P(q)$ and structure factor $S(q)$. The Guinier equation (Equation ESI-1) is essentially a form factor for a system of polydisperse objects of arbitrary shapes[3]. Approximating the structure factor as unity is valid for low concentrations of scatterers, as is easily understood from the most general form of the structure factor[3]:

$$S(q) = 1 + \langle n\rangle \int_0^\infty 4\pi r^2\{g(r) - 1\}\frac{\sin qr}{qr}\,dr \qquad \text{(ESI-3)}$$

where $<n>$ is the number density of particles. At higher concentrations $I(q)$ depends on the pair distribution function $g(r)$ describing the spatial distribution of particles. However, as long as there are no long-range interactions and particles cannot completely overlap, $S(q) < 1$ at small q and $S(q) \approx 1$ at high q. Thus if the maximum of $P(q)$ is at $q = 0$ (the case for the Guinier law as well as simple hard spheres), the effect of dense packing is to move this maximum to a finite wavevector[3] (Figure ESI-5).

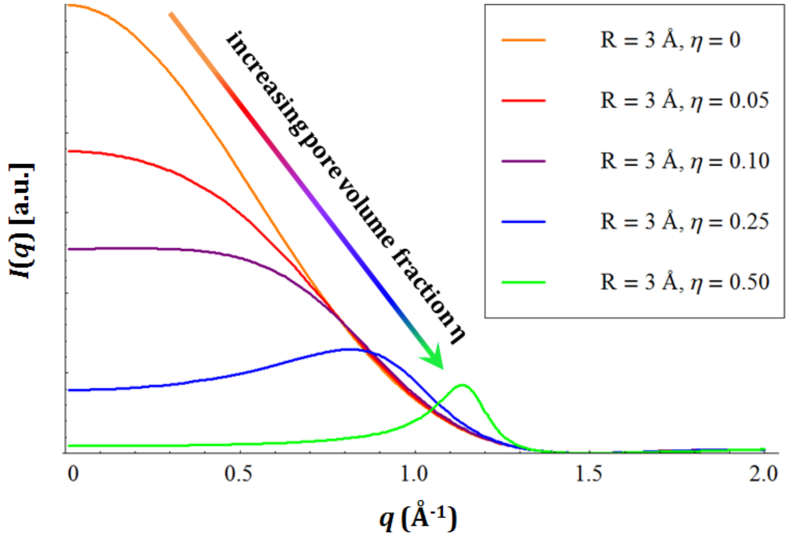

Figure ESI-5. Effect of pore volume fraction on scattered intensity from monodisperse, Percus-Yevick hard spheres with a constant radius.

Since particles are pores in this case, any 'interactions' between them arise indirectly through chain statistics and packing; it is difficult to predict what functional form this might take. Hard-sphere interactions are assumed as a default starting point: particles are not allowed to overlap but experience neither repulsive nor attractive forces. The form factor due to monodisperse hard spheres is given by[3]

$$P(q) = \rho_0^2 v^2 \frac{9(\sin qR - qR\cos qR)^2}{(qR)^6} \qquad \text{(ESI-4)}$$

where R is the sphere radius, v is the particle volume and ρ_0 is the scattering contrast between particle and matrix.

Because $g(r)$ depends on the particle volume fraction η, $S(q)$ is also a function of η and its derivation requires an assumption about the nature of many-body interactions known as a closure relationship. For hard spheres with liquid-like order, the Percus-Yevick closure has been broadly successful. (See for example ref [7] for a full discussion.) The resulting structure factor has a complex functional form, given in many sources but notably in ref [8] with no typographical errors:

$$S(q, R_{HS}, \eta_{HS}) = \frac{1}{1 + 24\eta_{HS} G(2R_{HS}q)/(2R_{HS}q)} \qquad \text{(ESI-5)}$$

where

$$G(A) = \frac{\alpha}{A^2}(\sin A - A\cos A) + \frac{\beta}{A^3}[2A\sin A - (2 - A^2)\cos A] + \frac{\gamma}{A^5}[-A^4\cos A + 4([3A^2 - 6]\cos A + [A^3 - 6A]\sin A + 6)] \tag{ESI-6}$$

and

$$\alpha = \frac{(1 + 2\eta_{HS})^2}{(1 - \eta_{HS})^4} \tag{ESI-7a}$$

$$\beta = -6\eta_{HS}\frac{\left(1 + \frac{\eta_{HS}}{2}\right)^2}{(1 - \eta_{HS})^4} \tag{ESI-7b}$$

$$\gamma = \frac{\eta_{HS}}{2}\alpha \tag{ESI -7c}$$

Here η_{HS} and R_{HS} are taken to be equal to the η and R that appear in the form factor, but various core-shell models exist in which spheres of size R interact with a larger or smaller effective radius R_{HS}.

Figure ESI-5 illustrates the effect of increasing pore volume fraction on the shape of the scattered intensity from hard spheres: a peak appears at finite q. In Figure ESI-6, the pore (particle) size is varied with the pore volume fraction fixed at a value of 0.25, a reasonable value for PIM-1. The peak moves to lower q when the pore radius is increased, like any scattering feature. However, because the peak position also depends on the pore volume fraction, it does not give a direct indication of pore size (e.g. $d = 2\pi/q$).

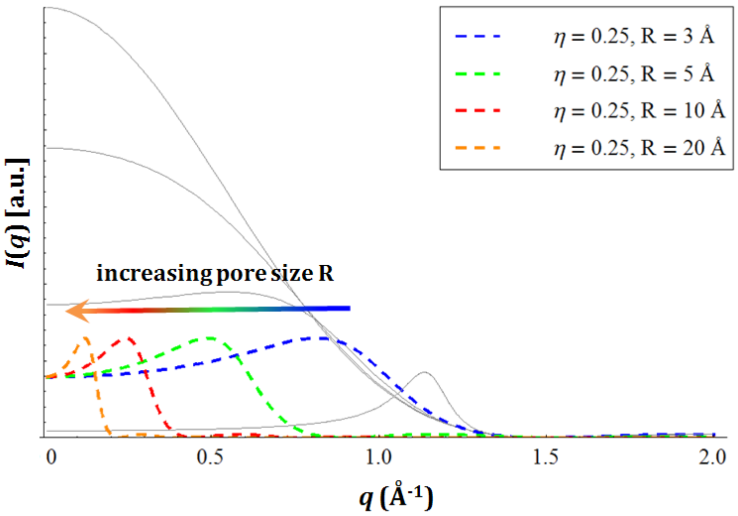

Figure ESI-6. Effect of pore size on scattered intensity from monodisperse hard spheres at a constant pore volume fraction. Other curves from Figure ESI-5 are shown in grey.

Comparing the hard-sphere model with experimental scattering data from PIM-1, the broad SAXS maximum can be reproduced with a volume fraction of 0.25 and pore radius of 10 Å (Figure ESI-7). Although this pore size is two to three times that expected from other characterization data (Section 1.3.2.1), these parameters are overall physically reasonable.

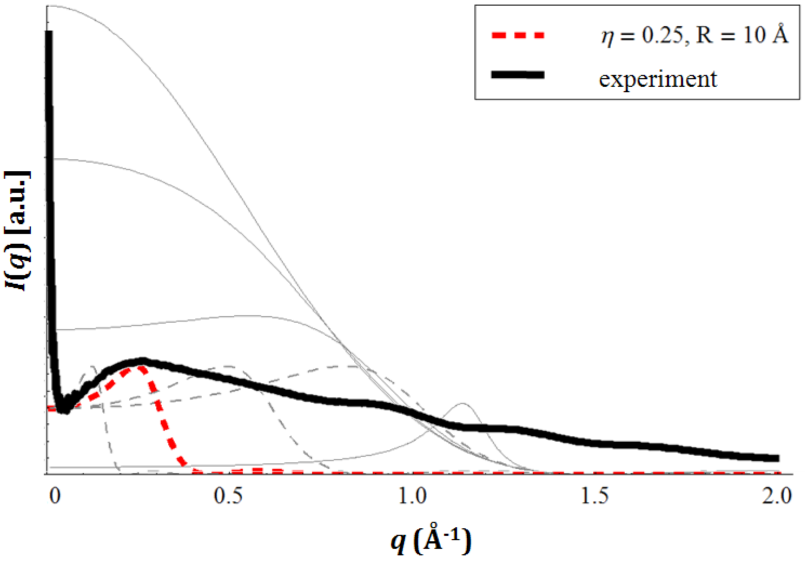

Figure ESI-7. Comparison of experimental PIM-1 scattering with scattering from monodisperse hard spheres with a radius of 10 Å at a volume fraction of 0.25. Other curves from Figures ESI-5 and ESI-6 are shown in grey.

The monodisperse hard-sphere model discussed up to this point fails to reproduce the breadth of the observed peak. Real pores are not monodisperse, and incorporating polydispersity increases the breadth of the peak while smearing out secondary maxima in the monodisperse form factor (Figure ESI-8). A ‘locally monodisperse’ model of polydispersity[9] previously applied to a system with larger pores[10] is used here. The form factor and structure factor are weighted by a pore size distribution $n(r)$ and integrated to yield the total intensity:

$$I(q) = \int_0^\infty n(R)P(q,R)S(q,R,\eta_{\text{total}})dR \qquad \text{(ESI-8)}$$

Although the high-q agreement is improved in the polydisperse model, the agreement with experimental data below the peak maximum is reduced (Figure ESI-8).

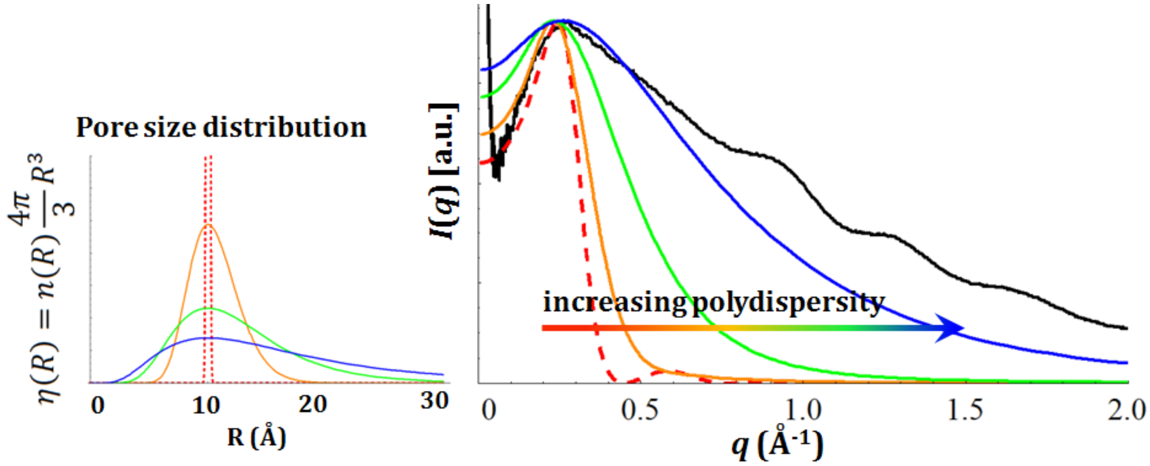

Figure ESI-8. Effect of polydispersity on scattered intensity from hard spheres using Equation ESI-8. Log-normal pore size distributions with a constant peak radius of 10 Å and constant total pore volume fraction of 0.25 of increasing polydispersity are shown at left with corresponding color-coded modeled scattering patterns at right. Experimental scattering from a PIM-1 film is shown in black.

The primary problem with this hard-sphere model, however, is larger apparent size of pores: scattering from pores of a 10-Å radius matches experimental data fairly well, but other structural measurements suggest that PIM-1 contains pores primarily smaller than 10 Å in diameter. Since pores have sizes only because their borders are defined by polymer segments, it could be postulated that pores interact with $R_{HS} > R$, with $(R_{HS} - R)$ related to the width of a polymer segment. However, it is also clear that the porosity in PIMs must be well-connected: permeability is high, but gas molecule transport cannot be facilitated by polymer mobility when segments do not move on the time scale of gas molecule motion. This means that many pore 'particles' are in direct contact, with $R_{HS} = R$. In addition, the decrease in pore volume fraction during aging could be described by interpenetrating pores with $R_{HS} < R$.

An accurate hard-sphere model would seem to require significant anisotropy, with pores interacting with an effective radius depending on their relative orientation: pores separated by a polymer segment would interact with $R_{HS} > R$, while pores able to contact one another would interact with $R_{HS} = R$. A model could account for changes in PIM scattering during aging by multiple mechanisms, including both shrinking pores and pores in direct contact ($R_{HS} = R$) gaining the ability to overlap ($R_{HS} < R$). Such a model would require several unmeasurable, arbitrary parameters. Considering hard-sphere models for porosity provides some basic insight and further support for the association of the broad SAXS maximum with porosity. However, such a model is not ideal for quantifying changes in PIM structure during aging.

ESI-2.3 Nonparticulate, Bicontinuous Teubner-Strey Model

In a nonparticulate system, there is no distinction between form factor and structure factor. Instead of the radial distribution function $g(r)$ that describes particulate systems, the real-space analog of scattered intensity from a nonparticulate two-phase system is the correlation function $\gamma(r)$, a Fourier transform of $I(q)$ normalized to 1 at $r = 0$[3]:

$$I(q) = 4\pi V\langle\eta^2\rangle \int_0^\infty \gamma(r) r^2 \frac{\sin qr}{qr} dr \qquad \text{(ESI-9)}$$

where $<\eta^2>$ is the mean square fluctuation in scattering length density. If the two phases are randomly distributed with a well-defined interface, then the correlation function takes an exponential form[5]*:*

$$\gamma(r) = e^{-r/\xi} \qquad \text{(ESI-10)}$$

where ξ is the correlation length appearing in the Debye-Bueche equation (Equation ESI-2). It is the assumption of this exponential form in Equation ESI-10 that leads to the absence of an intensity maximum in Equation ESI-2. Despite the validity of the Debye-Bueche equation for a number of non-polymeric porous materials even at a high volume fraction of pores[5], it can be inferred that the distribution of porosity (unoccupied volume) in PIMs is *not* random. This may be due to the fact that pores are simply the space not occupied by polymer chains; there are relatively few degrees of freedom in the configuration of a PIM chain, so there may be correlations in the locations of nearby pores.

The Debye-Bueche equation has been applied successfully to a wide variety of systems, and there are few examples of alternate functional forms of the correlation function. One example was derived by Teubner and Strey[11] for microemulsions, one example of which are bicontinuous mixtures of water and oil with a surfactant stabilizing the interface:

$$\gamma(r) = \frac{d}{2\pi r} e^{-r/\xi} \sin\frac{2\pi r}{d} \qquad \text{(ESI-11)}$$

corresponding to scattered intensity of the form

$$I(q) \propto \frac{1}{a_2 + c_1 q^2 + c_2 q^4} \qquad \text{(ESI -12)}$$

In addition to the correlation length ξ, a parameter d arises corresponding to a domain size or periodicity. In terms of the fit parameters, these are given by

$$\xi = \left[\frac{1}{2}\left(\frac{a_2}{c_2}\right)^{1/2} + \frac{1}{4}\frac{c_1}{c_2}\right]^{-1/2} \qquad \text{(ESI -13a)}$$

and

$$d = 2\pi \left[\frac{1}{2}\left(\frac{a_2}{c_2}\right)^{1/2} - \frac{1}{4}\frac{c_1}{c_2}\right]^{-1/2} \qquad \text{(ESI -13b)}$$

In the derivation of these equations, a_2, c_1, and c_2 are coefficients appearing in an order-parameter expansion of the free energy density. A maximum in scattered intensity as given by Equation ESI-12 requires $a_2 > 0$, $c_1 < 0$, $c_2 > 0$, and $4a_2c_2 - c_1^2 > 0$, corresponding to the thermodynamic characteristics of microemulsions.

Equation ESI-12 does not fit PIM-1 scattering patterns well (Figure ESI-9), primarily due to the fact that the peak breadth is coupled to the intensity at $q = 0$[11]. This is similar to a problem encountered with the hard-sphere model above: when polydispersity was introduced (Figure ESI-8), the model more accurately captured the peak breadth at high q, but the intensity of the model below the peak maximum increased, in poor agreement with experimental data.

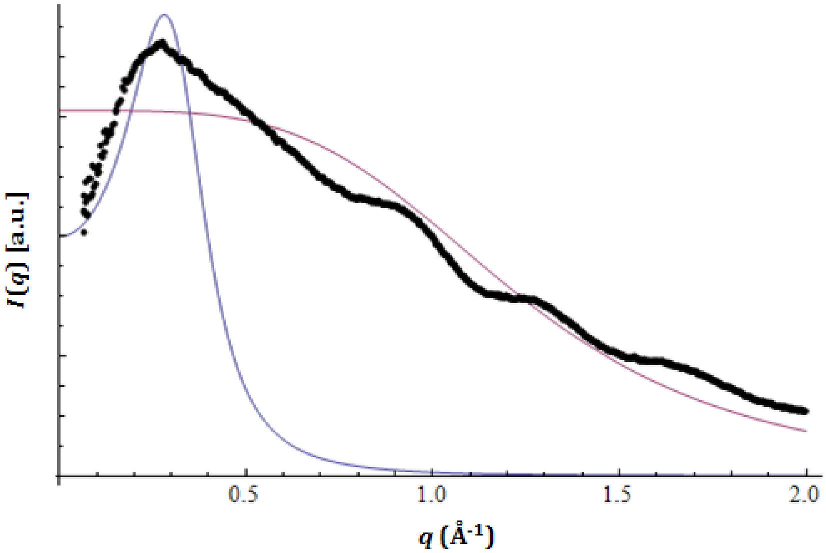

Figure ESI-9. Two least-squares Teubner-Strey model (Equation ESI-12) fits to a PIM-1 scattering pattern. Fitting the entire range of experimental data shown (black) with only the constraints listed above produces the mauve curve, which captures the breadth of the scattering pattern but not does reproduce the maximum (ξ = 1.1 Å, d = 7.3 Å). Using only data below 0.36 Å^{-1}, and constraining $I(0)$ to be no larger than the vertical axis intercept shown, produces the blue curve, which captures the peak location but is far too narrow (ξ = 7.6 Å, d = 20.2 Å).

In the two extreme versions of the Teubner-Strey model illustrated in Figure ESI-9, ξ ranges from 1.1 to 7.6 Å and d from 7.3 to 20.2 Å. These appear to be reasonable size scales for describing PIM porosity, but their meaning is unclear in this context. Space occupied by atoms and space not occupied by atoms (porosity) certainly constitute two ’phases’ in the sense that there is scattering length density contrast between them. However, it is questionable whether they can be treated as two phases in the usual thermodynamic sense. The observation of physical aging itself indicates that the system is not in equilibrium. In addition, the distribution of unoccupied volume is significantly influenced by atomic close-packing and connectivity constraints imposed by covalent bonds along polymer chains spanning large length scales compared to the size of pores.

Without further work to understand the meaning of the thermodynamic and structural parameters in the Teubner-Strey bicontinuous model, it is not ideal as a primary means of evaluating changes in PIM scattering patterns during aging. The fit of the model as developed for microemulsions is poor, but it could provide a starting point for further work.

ESI-3. PIM-1 AGING SAXS/WAXS PATTERNS

This appendix contains the separate SAXS and WAXS patterns which are shown merged in the aging section, 3.2. WAXS patterns are truncated at 1 Å^{-1} to focus on the SAXS/WAXS overlap region. Summary data computed from these patterns, including the partial scattering invariant and peak position, are reported in the main paper. Versions of these with alternate integration limits for the invariant calculation are also shown here.

All SAXS patterns were collected at room temperature with a sample-to-detector distance of 0.5 m and were calibrated to absolute intensity; it is important to note that this included normalization by sample thickness. WAXS patterns were scaled to overlap SAXS patterns.

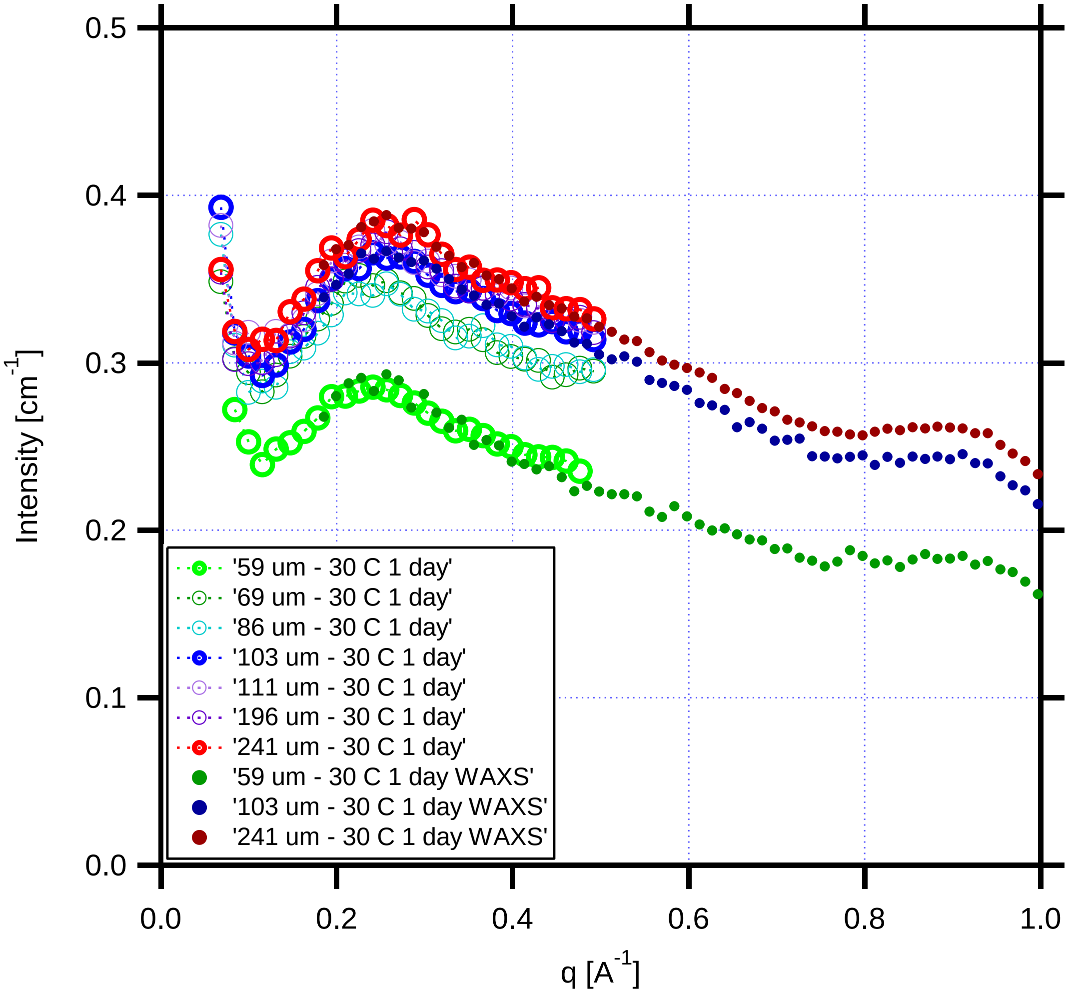

Figure ESI-11. SAXS (open circles) and WAXS (filled circles) patterns from PIM-1 films aged at 30 °C for 1 day after removal from ethanol.

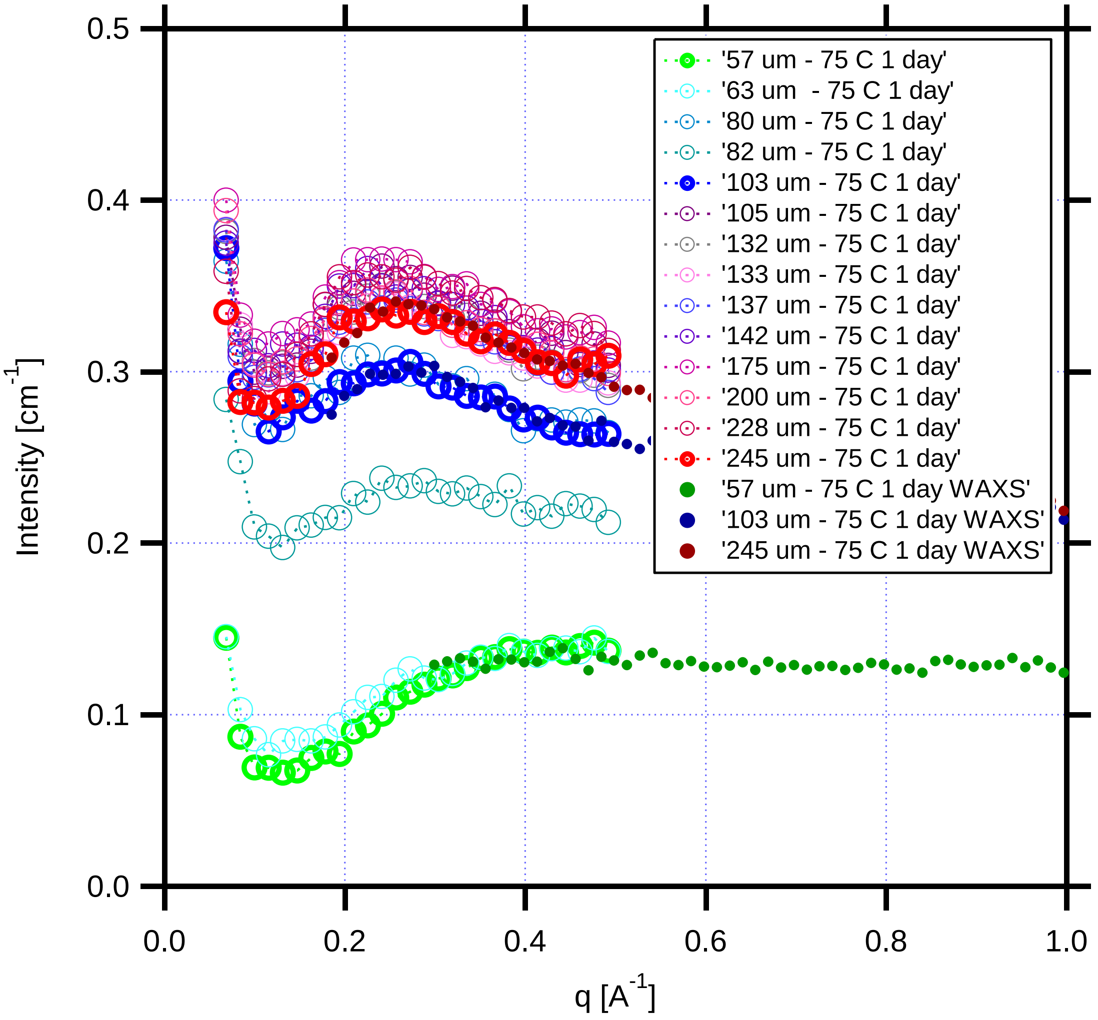

Figure ESI-12. SAXS (open circles) and WAXS (filled circles) patterns from PIM-1 films aged at 75 °C for 1 day after removal from ethanol.

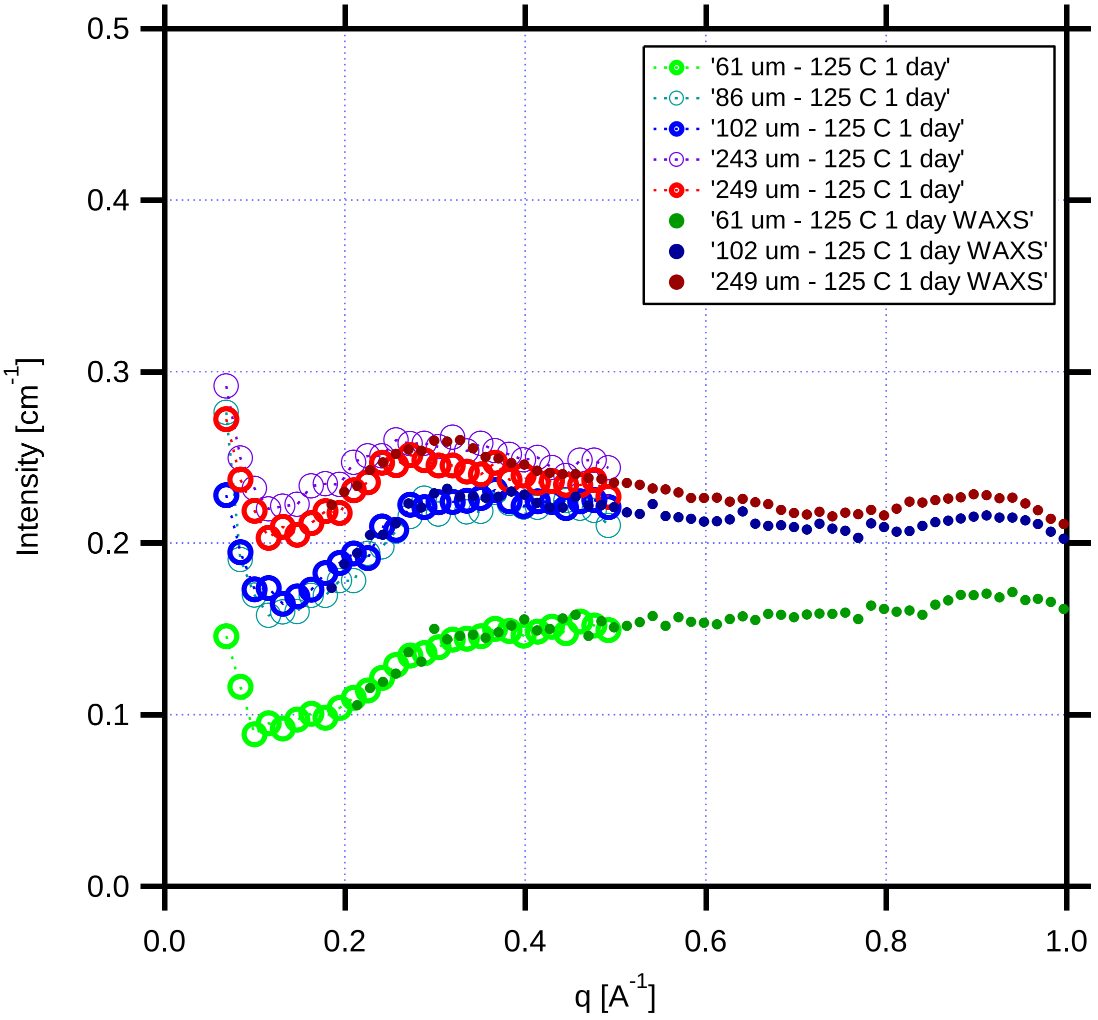

Figure ESI-13. SAXS (open circles) and WAXS (filled circles) patterns from PIM-1 films aged at 125 °C for 1 day after removal from ethanol.

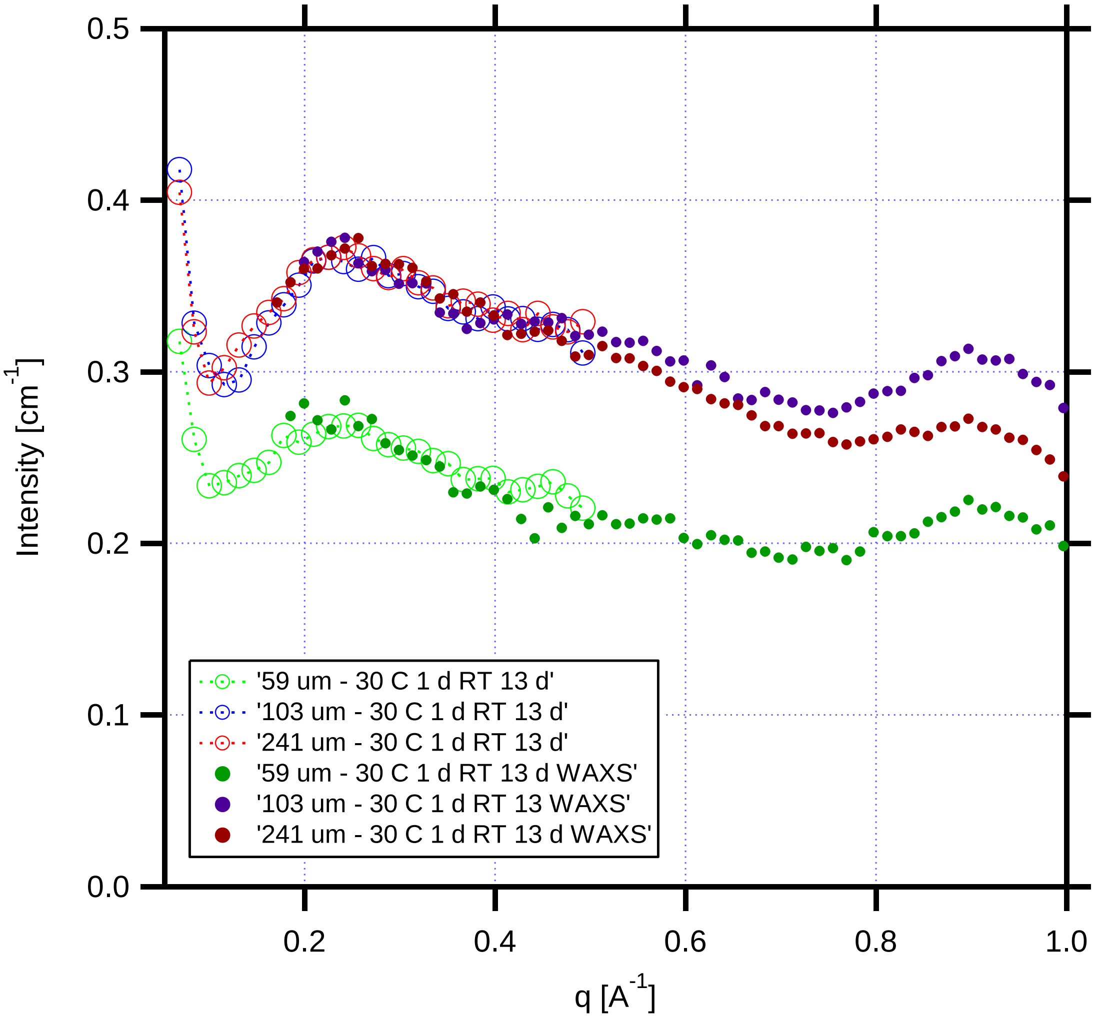

Figure ESI-14. SAXS (open circles) and WAXS (filled circles) patterns from PIM-1 films aged at 30 °C for 1 day (after removal from ethanol) and then for 13 days at ambient temperature in an evacuated DESI-Vac container.

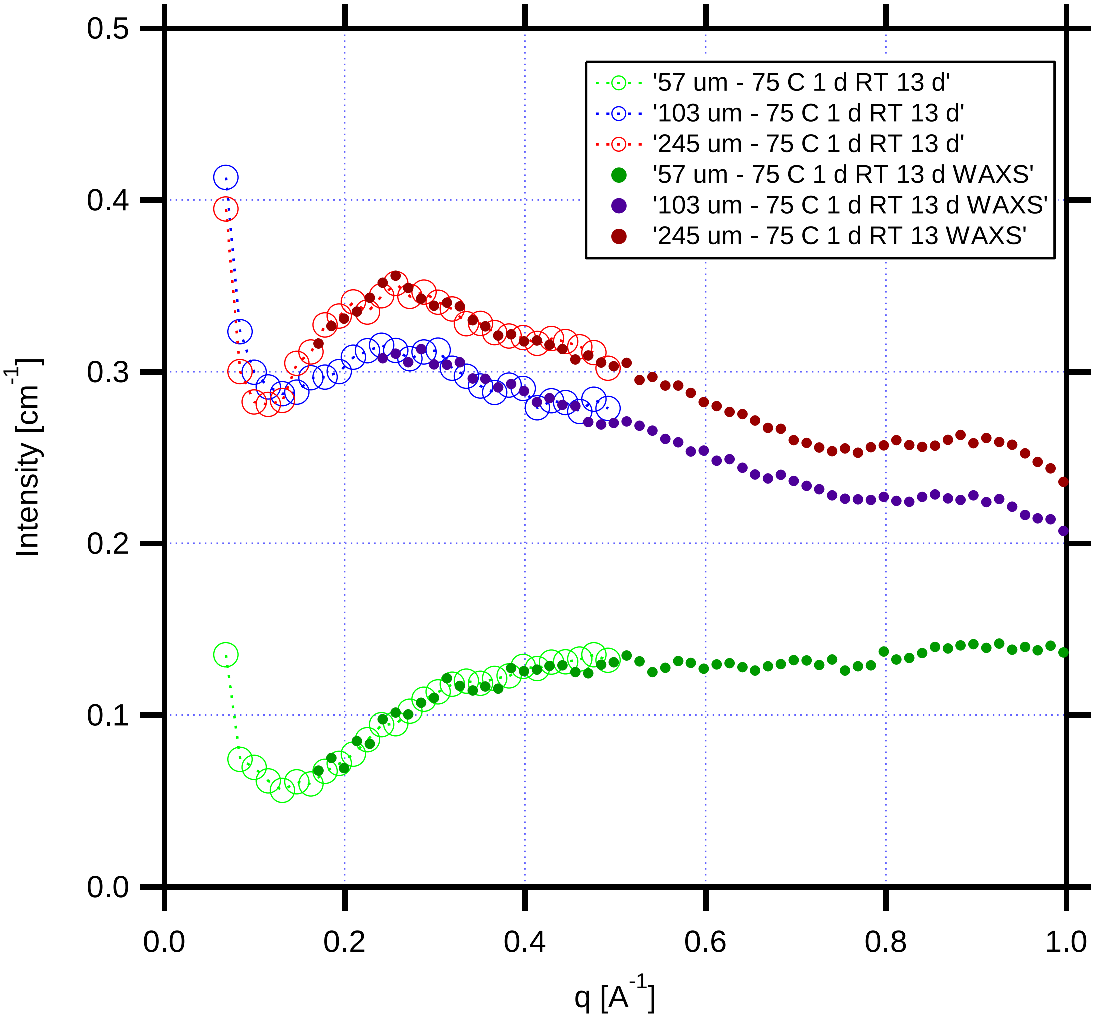

Figure ESI-15. SAXS (open circles) and WAXS (filled circles) patterns from PIM-1 films aged at 75 °C for 1 day (after removal from ethanol) and then for 13 days at ambient temperature in an evacuated DESI-Vac container.

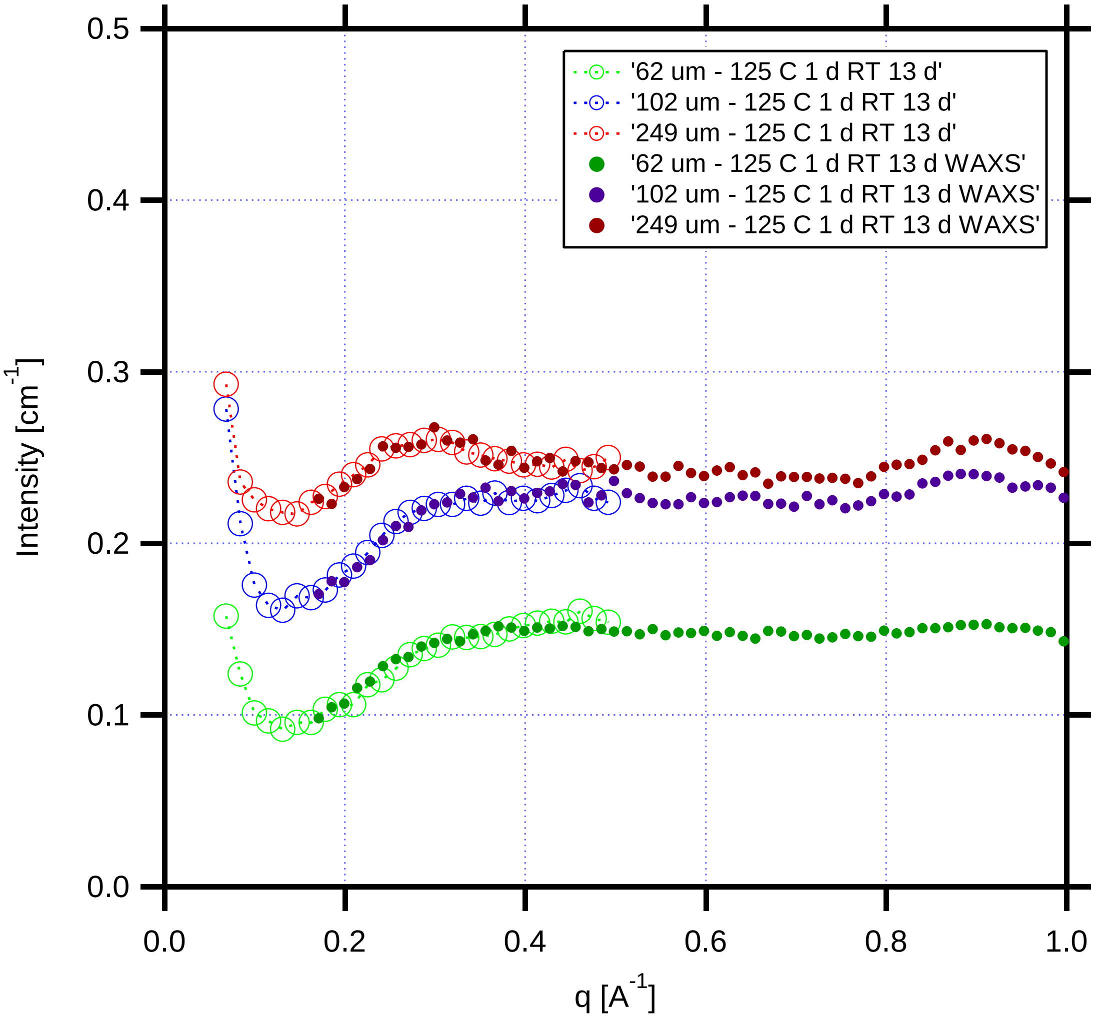

Figure ESI-16. SAXS (open circles) and WAXS (filled circles) patterns from PIM-1 films aged at 125 °C for 1 day (after removal from ethanol) and then for 13 days at ambient temperature in an evacuated DESI-Vac container.

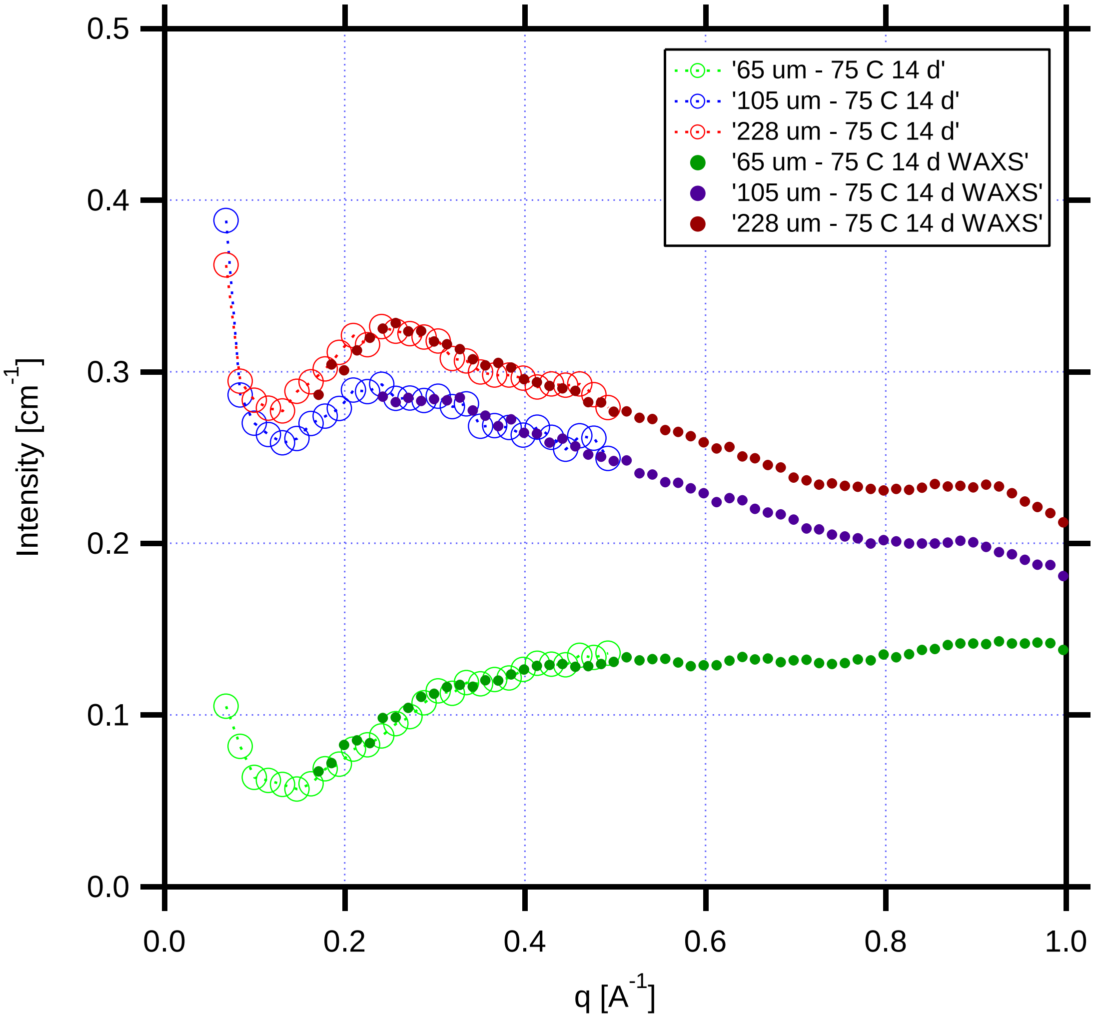

Figure ESI-17. SAXS (open circles) and WAXS (filled circles) patterns from PIM-1 films aged at 75 °C for 14 days (after removal from ethanol).

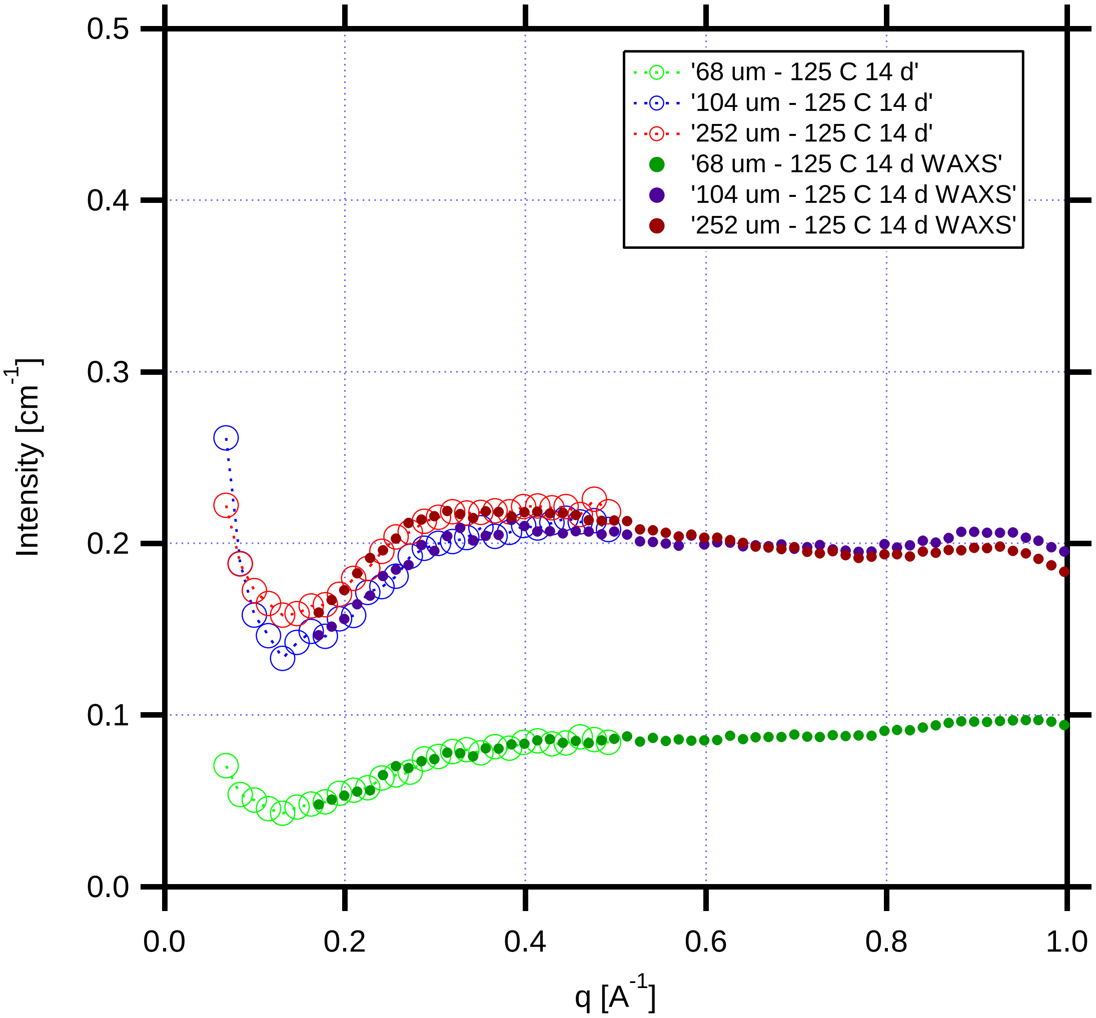

Figure ESI-18. SAXS (open circles) and WAXS (filled circles) patterns from PIM-1 films aged at 125 °C for 14 days (after removal from ethanol).

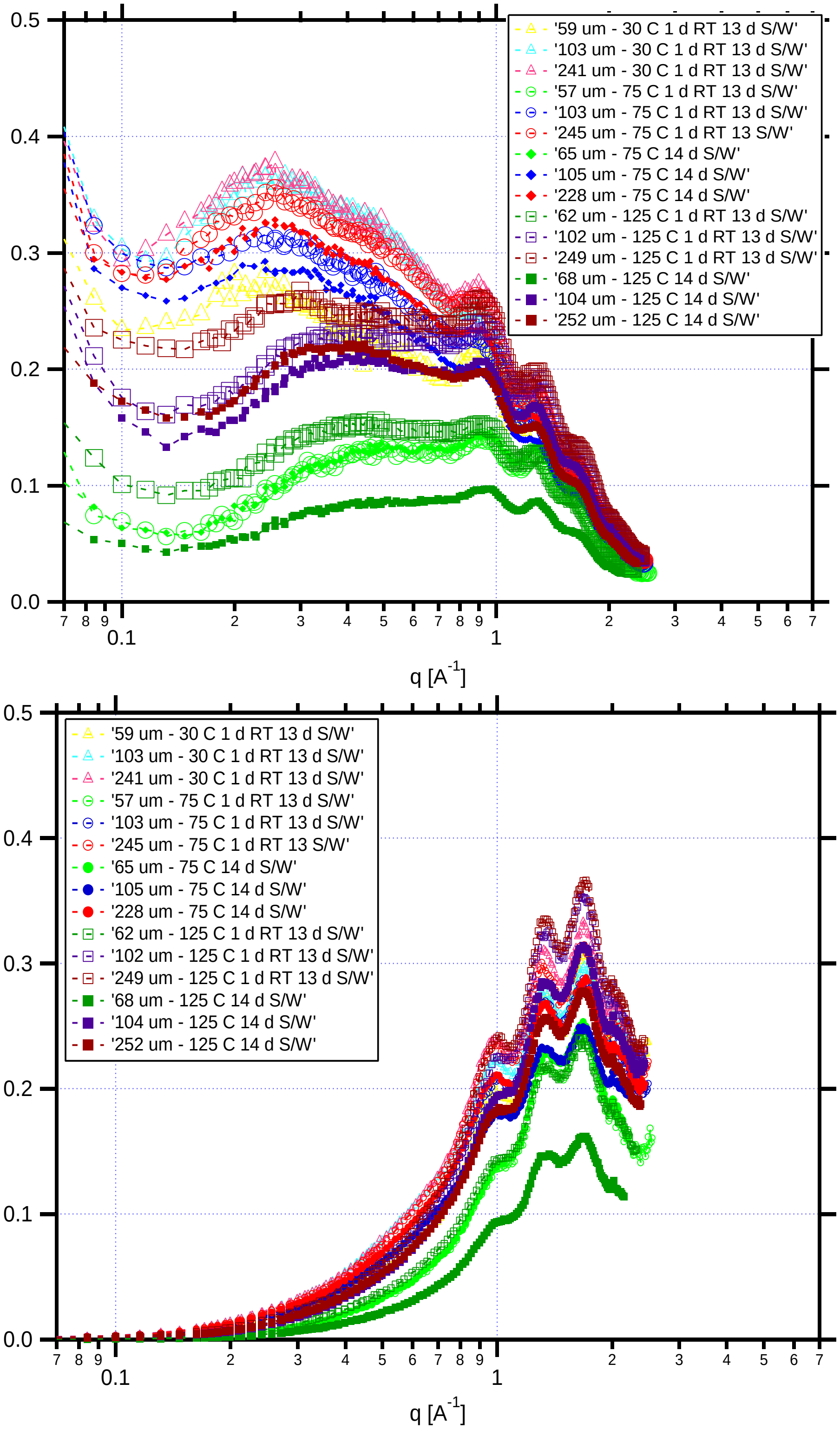

Figure ESI-19. Combined SAXS/WAXS patterns for films measured after two weeks (top) and contribution to the scattering invariant (bottom), analogous to Figure 8 (main text).

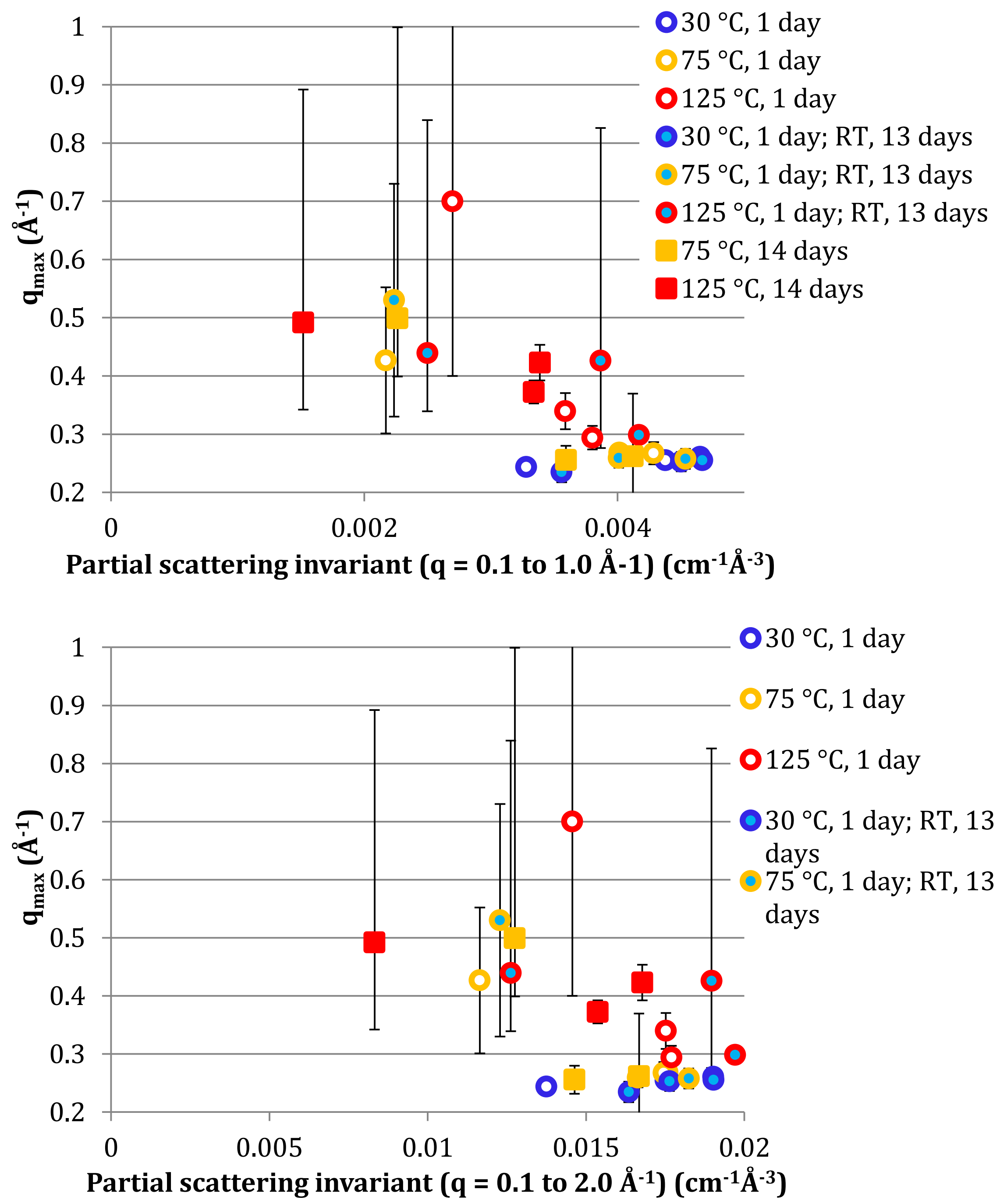

Figure ESI-20. SAXS/WAXS wavevector maxima plotted versus the scattering invariant with alternate upper integration limits of 1.0 Å^{-1} (top) and 2.0 Å^{-1} (bottom).

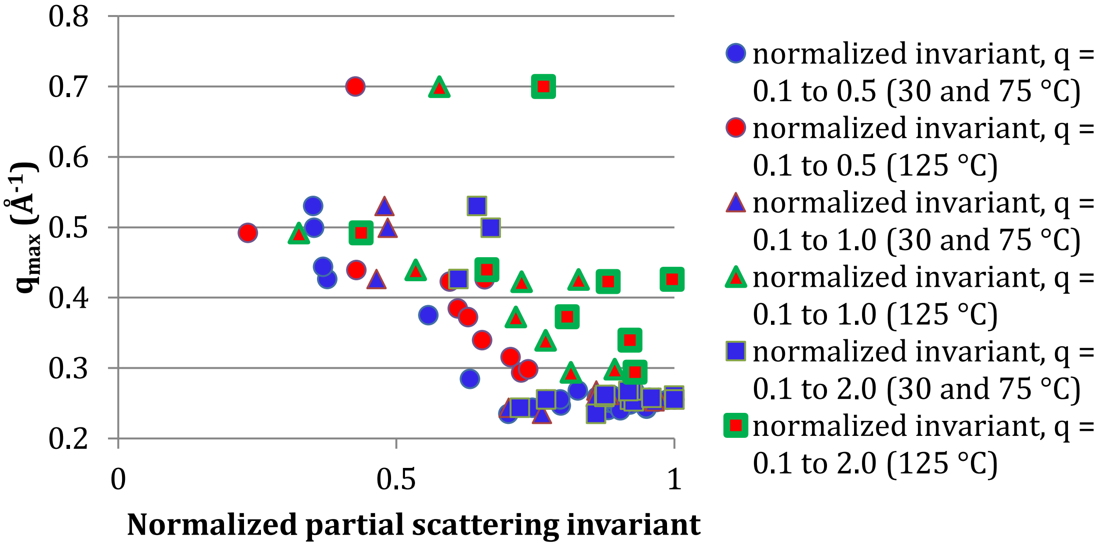

Figure ESI-21. SAXS/WAXS wavevector maxima plotted versus the scattering invariant with three different upper integration limits, normalized by the maximum value of the invariant. Deviations from the behavior highlighted in Figure 11 (main text) occur only in films exposed to temperatures of 125 °C (red symbols) and only with invariant upper integration limits of 1.0 or 2.0 Å^{-1} (green border).

ESI-4. DETAILS OF MOLECULAR DYNAMICS SIMULATIONS

Ten cubic boxes were created, each initially 124 Å in length. Each was packed with 64 randomly grown PIM-1 chains, with each chain 10 monomers in length, resulting in an initial density of 0.25 g/cm^3. Each box contained 22656 atoms, with $-CH_3$ and $-CH_2$ groups counted as single atoms in the united-atom scheme. Each box was then subjected to the compression scheme[12] in Table ESI-2, using the same force field and charges as ref [12]. In the configurations marked with an asterisk (*), surface areas and simulated X-ray scattering patterns were calculated as reported in the main text, averaged over 11 configurations sample at evenly spaced time intervals during the stage. Pore size distributions were calculated from the final configuration in each stage. All quantities reported in the main text were averaged over these 10 boxes.

Table ESI-2. Surface area and density of 81-Å PIM-1 boxes during compression and decompression[12]. Error bars represent the standard deviation over 10 boxes.

Stage	Duration (ps)	Ensemble	Temp (K)	Pressure (bar)	Avg. box size (Å)	St. dev. box size (Å)	Avg. density (g/cm^3)	St. dev. density (g/cm^3)	Nominal pressure (NVT)
0		NVT							
1	50	NVT	600						
2	50	NVT	300						
3	50	NPT	300	1000					
4	50	NVT	600						
5a	50	NVT	300						
5b*	50	NVT	300		79.21	0.19	0.997	0.007	1000 bar
6	50	NPT	300	30000					
7	50	NVT	600						
8a	50	NVT	300						
8b*	50	NVT	300		69.69	0.04	1.463	0.002	30000 bar
9	50	NPT	300	50000					
10	5	NVT	600						
11a	5	NVT	300						
11b*	5	NVT	300		68.11	0.02	1.568	0.002	50000 bar
12	5	NPT	300	25000					
13	5	NVT	600						
14a	5	NVT	300						
14b*	5	NVT	300		70.05	0.03	1.441	0.002	25000 bar
15	5	NPT	300	5000					
16	5	NVT	600						
17a	5	NVT	300						
17b*	5	NVT	300		75.14	0.12	1.167	0.006	5000 bar
18	5	NPT	300	500					
19	5	NVT	600						
20a	5	NVT	300						
20b*	5	NVT	300		79.43	0.31	0.988	0.011	500 bar
21	800	NPT	300	1					
22*	50	NVT	300		80.73	0.23	0.941	0.008	1 bar

REFERENCES

1. A. G. McDermott, G. S. Larsen, P. M. Budd, C. M. Colina and J. Runt, *Macromolecules*, 2011, **44**, 14-16.
2. M. Carta, K. J. Msayib, P. M. Budd and N. B. McKeown, *Organic letters*, 2008, **10**, 2641-2643.
3. R.-J. Roe, *Methods of X-Ray and Neutron Scattering in Polymer Science*, Oxford University Press, New York, 2000.
4. *Handbook of Porous Solids*, Wiley-VCH, 2002.
5. P. Debye, H. R. Anderson Jr and H. Brumberger, *Journal of applied Physics*, 1957, **28**, 679.
6. P. Debye and A. M. Bueche, *Journal of applied Physics*, 1949, **20**, 518-525.
7. J.-P. Hansen and I. R. McDonald, *Theory of Simple Liquids*, Academic Press, 2006.
8. D. J. Kinning and E. L. Thomas, *Macromolecules*, 1984, **17**, 1712-1718.
9. J. S. Pedersen, *Journal of Applied Crystallography*, 1994, **27**, 595-608.
10. E. Huang, M. F. Toney, W. Volksen, D. Mecerreyes, P. Brock, H. C. Kim, C. J. Hawker, J. L. Hedrick, V. Y. Lee, T. Magbitang, R. D. Miller and L. B. Lurio, *Applied Physics Letters*, 2002, **81**, 2232-2234.
11. M. Teubner and R. Strey, *The Journal of Chemical Physics*, 1987, **87**, 3195-3200.
12. G. S. Larsen, P. Lin, K. E. Hart and C. M. Colina, *Macromolecules*, 2011, **44**, 6944-6951.